


Fe-HCOF-PEG²⁰⁰⁰ as a Hypoxia-Tolerant Photosensitizer to Trigger Ferroptosis and Enhance ROS-Based Cancer Therapy

Hui Peng^{1,2,*}, Qian Jiang^{1,*}, Wenhao Mao^{1,3,*}, Zhonglan Hu^{1,*}, Qi Wang⁴, Zhuo Yu¹, Li Zhang¹, Xinyan Wang⁵, Chunbo Zhuang¹, Jia Mai⁶, Zhiyuan Wang⁷, Ting Sun¹ 

¹Department of Clinical Laboratory, The First Affiliated Hospital of Zhengzhou University, Zhengzhou, 450052, People's Republic of China; ²Center for Clinical Laboratory, General Hospital of the Yangtze River Shipping Wuhan Brain Hospital, Wuhan, Hubei, 430010, People's Republic of China; ³Department of Oncology, The First Affiliated Hospital of Zhengzhou University, Zhengzhou, 450052, People's Republic of China; ⁴Department of Pharmacy, Kaifeng Hospital of Traditional Chinese Medicine, Kaifeng, 475000, People's Republic of China; ⁵Department of Obstetrics, The First Affiliated Hospital of Zhengzhou University, Zhengzhou, 450052, People's Republic of China; ⁶Department of Laboratory Medicine, West China Second Hospital, Sichuan University, Chengdu, 610041, People's Republic of China; ⁷Henan Institute of Advanced Technology, Zhengzhou University, Zhengzhou, 450001, People's Republic of China

*These authors contributed equally to this work

Correspondence: Ting Sun, Department of Clinical Laboratory, The First Affiliated Hospital of Zhengzhou University, Zhengzhou, 450052, People's Republic of China, Email sunting@zzu.edu.cn; Zhiyuan Wang, Henan Institute of Advanced Technology, Zhengzhou University, Zhengzhou, 450001, People's Republic of China, Email wangzhiyuan@zzu.edu.cn

Background: The hypoxic tumor microenvironment and single mechanisms severely limit the photodynamic therapy (PDT) efficiency of covalent organic framework (COF) nanoparticles in cancer treatment.

Purpose: Here, we propose an iron-loaded, hydrophilic 1,2-distearoyl-sn-glycero-3-phosphoethanolamine-N-[methoxy(polyethylene glycol)-2000] (DSPE-PEG2000)-modified hollow covalent organic framework (HCOF), Fe-HCOF-PEG²⁰⁰⁰, for use in hypoxic PDT and ferroptosis therapy owing to its type I and II photodynamic ability and iron nanoparticle loading property.

Results: Fe-HCOF-PEG²⁰⁰⁰ nanoparticles (Fe-HCOFs-PEG²⁰⁰⁰) with semiconducting polymers and microporous skeletons allow efficient photophysical properties. Moreover, the iron nanoparticles on Fe-HCOF-PEG²⁰⁰⁰ caused ferroptosis and further enhanced tumor elimination under normoxic and hypoxic conditions. DSPE-PEG²⁰⁰⁰ endowed Fe-HCOF-PEG²⁰⁰⁰ with hydrophilicity, allowing it to circulate and accumulate in organs rich in blood supply, especially tumors. 808 nm NIR activated Fe-HCOF-PEG²⁰⁰⁰ aggregated in tumors and significantly inhibited tumor growth under hypoxia.

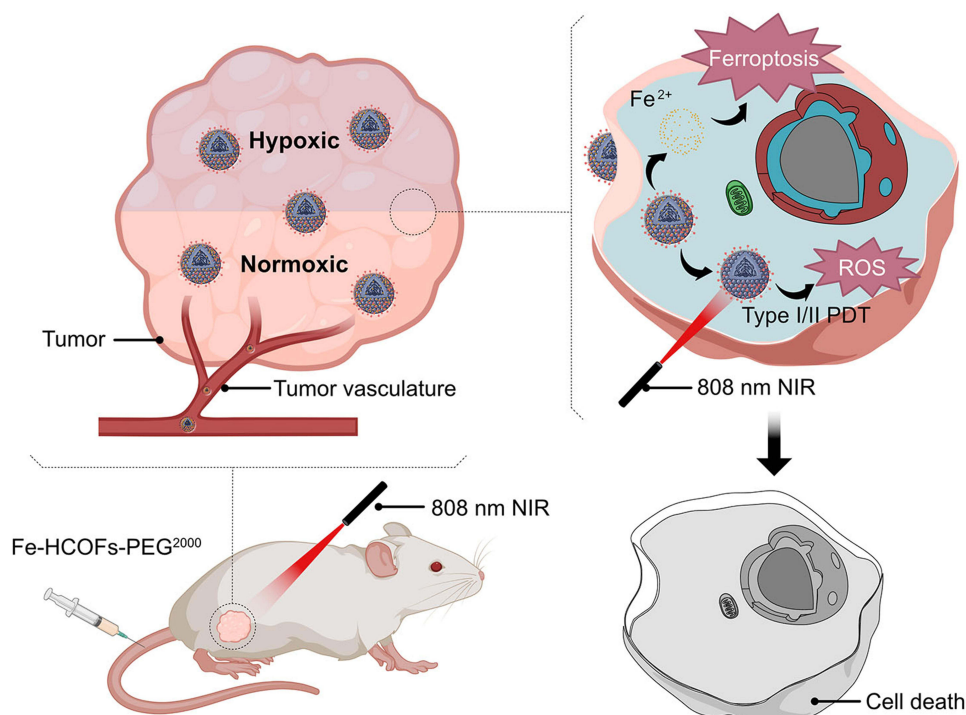
Conclusion: To our knowledge, Fe-HCOF-PEG²⁰⁰⁰ is the leading combination of type I/II PDT and ferroptosis. The strong antitumor effects of this nanomaterial suggest prospects for clinical translation as a tumor nanotherapy drug.

Keywords: HCOFs, PDT, ROS, hypoxia, ferroptosis, cancer cells

Introduction

Photodynamic therapy (PDT) is a universal and promising type of noninvasive tumor therapy that uses the cytotoxicity of reactive oxygen species (ROS) produced by photosensitizers (PSs) to kill cancer cells.^{1,2} Traditional PSs rely on the type II photodynamic effect, exciting oxygen into singlet oxygen (¹O₂) through the electron transfer process after exposure to light energy.³ Therefore, oxygen is a prerequisite element for type II PDT. However, the rapid growth and metabolism of cancer cells consume a large amount of oxygen from the blood, resulting in a hypoxic tumor microenvironment. The need for oxygen during photodynamic reactions greatly limits the clinical efficacy of PDT.⁴ Therefore, research on photodynamic nanomaterials with combined effects and photosensitive nanomaterials that can overcome, utilize, or tolerate hypoxic environments has attracted much attention.⁵ While most strategies to increase the effect of PDT focus on the oxygen supply in tumors, the improvements are limited and short lasting. Recently, researches on PSs that perform

Graphical Abstract



type I PDT have demonstrated their superiority in tumor treatment owing to their diminished oxygen dependence.⁶ However, most PSs can only excite molecular oxygen to produce $O_2^{\cdot-}$, which requires an oxygen supply and limits ROS generation. PSs that transfer energy, electrons, and hydrogen to simultaneously generate O_2 , H_2O , H^+ , and H_2O_2 can produce a wider variety of ROS without oxygen limitation and exert a stronger cytotoxic effect.

Covalent organic frameworks (COFs) are a category of porous crystalline composed of periodic combinations of covalent bonds that form arranged organic molecules. COFs comprise various covalent organic polymers (COPs) with light elements to form different 2D and 3D structures. Extensive applications of COFs have been reported in multiple fields, including substance storage and separation, proton conduction, catalysis, molecular imaging, and sensing.^{7–10} Recently, the emergence and exploitation of COFs have contributed to medical development and cancer therapy.^{11–13} COFs have low cytotoxicity, high biocompatibility, and excellent stability,¹⁴ which allows COFs to exist in the physiological environment for a long time. Biomedical applications and biocompatible demonstrations of COFs have been reported for years, including drug and gene delivery, photodynamic and photothermal therapy in vitro or even in vivo.¹⁵ However, further evidence regarding their distribution in the body and accumulation in tumors is urgently needed. Owing to their porosity, COFs can be used for efficient drug delivery by encapsulating diverse cargos and controllable drug release in response to external stimuli.^{16,17} By encapsulating PSs in a robust framework, COFs are imbued with photodynamic characteristics.^{18,19} Nevertheless, this procedure was not found to improve the effect of the PS. COFs containing photosensitive structural blocks²⁰ and π - π conjugated structures²¹ can be directly used as PSs. However, the ROS generation of these COF nanomaterials is simple and inefficient. Improving the targeted aggregation of PSs is another starting point for improving their effectiveness. Biomimetic modification of PSs endows them with prolonged blood circulation and effective tumor lesion targeting ability. Cell membrane camouflaged PSs and amphiphilic material modified PSs have been widely utilized in tumor therapy.^{22,23} Moreover, clinically applied PSs absorb at wavelengths of 650–750 nm, and due to the scattering of laser light by the skin and other tissue, deeper tissues receive less light energy.²⁴ PSs that can be excited by longer wavelengths, such as near-infrared (NIR, 650–1000 nm)

wavelengths, are more clinically effective because of their greater penetration. Consequently, new NIR irradiation excited COF nanomaterials with sufficient ROS production and no oxygen restriction are urgently needed.

PDT treatment exerts its antitumor effects primarily by inducing cell apoptosis. However, emerging evidence suggests that tumor cells exhibit both inherent and acquired resistance against apoptosis.²⁵ Ferroptosis is a newly identified iron-dependent cell death process characterized by the accumulation of lipid peroxides and morphological changes in the mitochondria.²⁶ It has recently attracted increasing amounts of attention as a potential tumor-suppressing strategy.^{27–29} Ferroptosis induction depends on the imbalance of iron and mitochondrial metabolism, fatty acid-containing phospholipid synthesis, and the glutathione peroxidase 4 (GPX4) pathway. Alterations of the hallmarks of these systems, such as ferritin, cystine transporter solute carrier family 7 member 11 (SLC7A11), GPX4 and Acyl-CoA synthetase long-chain family member 4 (ACSL4), have been proven to facilitate tumor.³⁰ Excitingly, ferroptosis-inducing strategies propose new targets and overcome resistance to conventional therapies, including chemotherapy, radiotherapy, and even targeted therapies.^{31,32} With the inherent ability to interfere with critical molecules of ferroptosis and to precisely target cancer cells, nanoparticles present new prospects for precise cancer treatment. In a recent study, nanoparticles that release Fe^{2+} ions regulate crucial molecules involved in ferroptosis^{33,34} and carry small-molecule drugs^{35,36} that induce ferroptosis were found to present new opportunities for ferroptosis therapy and exhibited encouraging efficacy.

Moreover, PDT compensates for the shortcomings of ferroptosis to increase therapeutic efficacy and inhibit tolerability. ROS bursts are a well-established hallmark of ferroptosis, and recent studies have highlighted hypoxia as an inhibitor of ferroptosis.^{37,38} Once a tumor reaches a relatively large volume, the tumor center becomes an extremely hypoxic microenvironment because of limited angiogenesis and oxygen overconsumption. Therefore, ferroptosis-induced tumor cell death *in vivo* is inhibited in a hypoxic environment. The combination of oxygen-independent PDT with ferroptosis could overcome the limitations of ferroptosis therapy in tumors. However, no study has yet demonstrated the ferroptosis-inducing ability of nanomaterials in hypoxic environments.

Here, we present a new type of hollow structured covalent organic framework (HCOF) coordinated with iron and DSPE-PEG2000, known as Fe-HCOF-PEG²⁰⁰⁰. Fe-HCOF-PEG²⁰⁰⁰ nanoparticles (Fe-HCOFs-PEG²⁰⁰⁰) exhibit excellent photodynamic efficacy even under hypoxia. Due to the outstanding intermolecular electron transfer excited by 808 nm NIR light, Fe-HCOF-PEG²⁰⁰⁰ can generate substantial types and levels of lethal ROS even under low oxygen concentrations, overcoming the low efficiency of conventional PDT in the hypoxic microenvironment. The low-valence ions carried by Fe-HCOF-PEG²⁰⁰⁰ are absorbed into the cytoplasm to form a labile iron pool, which promotes lipid peroxidation, ultimately intensifying ferroptosis. In addition, we verified that Fe^{2+} and ROS-induced ferroptosis also occurred in hypoxic environments. Moreover, according to the experimental results, DSPE-PEG²⁰⁰⁰-modified Fe-HCOF can circulate safely *in vivo* and accumulate efficiently in tumors. Accordingly, we conclude that Fe-HCOF-PEG²⁰⁰⁰ has the potential as a therapeutic platform for efficient PDT and ferroptosis therapy in cancer.

Materials and Methods

Materials

1,3-Diphenylisobenzofuran (DPBF) was purchased from J&K Scientific Reagent. Dihydroethidium (Hydroethidine) and DCFH-DA (H2DCFDA) were purchased from Glpbio. Cell Counting Kit-8 (CCK-8) reagent was purchased from Uelandy. Reactive Oxygen Species Assay Kit, Lipid Peroxidation MDA Assay Kit, and JC-1 probe were purchased from Beyotime. Calcein-AM, Propidium iodide (PI), and Annexin V-FITC/PI Apoptosis Detection Kit were purchased from Yeason. HIF1- α , TUNEL, and GAPDH antibody (Mouse monoclonal) were purchased from Abcam. GPX4, SLC7A11, ACSL4, and Ferritin antibody (Rabbit monoclonal) were purchased from Abmart. HRP goat anti-mouse IgG and HRP goat anti-rabbit IgG were purchased from proteintech group. Relevant instrument parameters were supplemented in [Instrument parameters](#) (Supporting Information).

Synthesis of Fe-HCOFs and Fe-HCOFs-PEG2000

N,N-bis(4-aminophenyl)benzene-1,4-diamine (TAPA, 0.04 mmol) and 1,3,5-benzenetricarbaldehyde (BTCA, 0.04 mmol) (TAPA: BTCA = 1: 1) were added to the EP tubes, respectively, then acetonitrile (ACN) was added to resolve the above

chemicals completely and blended each other to obtain clear solution. Then, glacial acetic acid (Hac, 0.5 mL) was added to the above liquid immediately and stirred at room-temperature for 6 h. The yellow covalent organic polymers (COPs) were formed at the bottom of EP tubes. After being washed with anhydrous ethanol and 1,4-dioxane, the obtained COPs were re-dispersed in a mixture of 1,4-dioxane, trimethylbenzene (4:1 v/v), glacial acetic acid, and water, which were sealed and aged at 70°C for 2 days. Then a center amount of $\text{FeCl}_2 \cdot 4\text{H}_2\text{O}$ (0.01 mol l^{-1}) was added and stirred for another 2 h, followed by adding excess sodium borohydride solution (0.01 mol l^{-1}) under vigorous agitation. After 2 h, the precipitate was collected by centrifugation and washed with tetrahydrofuran and ethanol for several times. Then the Fe-HCOFs were obtained after drying at 80°C for 6 h. 10 mg Fe-HCOFs were dispersed in 5 mL PBS by ultrasound, then 5 mL PBS containing 20 mg DSPE-PEG2000 were added in it. After ultrasonic treatment, the mixture is centrifuged to extract the precipitate to get Fe-HCOFs-PEG²⁰⁰⁰.

Superoxide Anion Radical ($\text{O}_2^{\cdot-}$) Detection

Fe-HCOFs-PEG²⁰⁰⁰ was homogeneously dispersed in methanol which contains 100 μM DMPO to form 200 $\mu\text{g mL}^{-1}$ solution. Then the mixture was treated by intense ultrasound for 60 s and half of the mixture was taken as 0 min group. Another half was irradiated at 808 nm for 10 min (1.0 W cm^{-2}) and transferred to a quartz tube for EPR (Electron paramagnetic resonance). DHE was used to detect the generated $\text{O}_2^{\cdot-}$ by Fe-HCOFs-PEG²⁰⁰⁰ at 808 nm. 200 μg Fe-HCOFs-PEG²⁰⁰⁰, 50 μM DHE and 250 μg ctDNA were added to 1 mL NaAc buffer (0.01M, pH = 7.0) solution at room temperature. The mixture was irradiated by 808 nm NIR (1.0 W cm^{-2}) for designated time and then detect the 610 nm fluorescence by UV-vis spectrophotometer (Strictly avoid light during operation).

Hydroxyl Radical (OH^\bullet) Detection

Fe-HCOFs-PEG²⁰⁰⁰ were homogeneously dispersed in 0.01 M NaAc buffer (pH = 7.0) which contains 100 μM DMPO to form 200 $\mu\text{g mL}^{-1}$ solution. Then the mixture was subjected to intense ultrasound for 60 s. Half of the mixture was taken as 0 min group. Another half was irradiated at 808 nm for 10 min (1.0 W cm^{-2}) and transferred to a quartz tube for EPR.

Singlet Oxygen ($^1\text{O}_2$) Detection

Fe-HCOFs-PEG²⁰⁰⁰ were homogeneously dispersed in 0.01M NaAc buffer (pH = 7.0) which contains 100 μM TEMPO to form 200 $\mu\text{g mL}^{-1}$ solution. Then the mixture was subjected to intense ultrasound for 60 s. Half of the mixture was taken as 0 min group. Another half was irradiated at 808 nm for 10 min (1.0 W cm^{-2}) and transferred to a quartz tube for EPR.

Reactive Oxygen Species (ROS) Detection

Fe-HCOFs-PEG²⁰⁰⁰ were homogeneously dispersed in 0.01 M NaAc buffer which contains 1 μM DCFH-DA to form 200 $\mu\text{g mL}^{-1}$ solution. The buffer containing the same concentration of DCFH was used as the control group. Then the mixture was exposure to 808 nm (1.0 W cm^{-2}) for designated time, the fluorescence intensity and fluorescence spectrum of the solution at 525 nm were measured by UV-vis spectrophotometer after (Strictly avoid light during operation).

Cell Culture

The mouse breast cancer cell line 4T1 and the human breast cancer cell line MCF-7 were obtained from ATCC and cultured in 1640 medium and DMEM medium, respectively. These media were supplemented with 10% FBS and 1% penicillin/streptomycin and maintained at 37°C in Thermo Scientific CO₂ incubator. (Normoxia environment contains 20% O₂ and 5% CO₂, hypoxia environment contains 1% O₂, 5% CO₂).

Cellular Uptake

4T1 and MCF-7 cells were seeded and cultured in 6-well plates at equal density for 12 h. Subsequently, the culture medium was replaced with 200 $\mu\text{g mL}^{-1}$ Fe-HCOFs-PEG²⁰⁰⁰ for incubation at different time (0, 3, 6, 12, 24 h). After being washed by PBS, cells were centrifuged to detect the presence of Fe element by Inductively Coupled Plasma-Mass Spectrometry (ICP-MS).

Cell Viability Assay

4T1 and MCF-7 cells were seeded and cultured in 96-well plates at a density of 6000 well⁻¹ for 12 h. The cells were treated with the indicated concentrations (0, 12.5, 25, 50, 100, 150, 200 µg mL⁻¹) of Fe-HCOFs-PEG²⁰⁰⁰ nanomaterials for 12 h, followed by exposure under 808 nm near infrared laser (1.0 W cm⁻² for 5 min), then another 12 h under either normoxic or hypoxic conditions. Cell viability was measured by CCK-8 assay. The absorbance of both the experimental group (A₀) and the control group (A_C) at 450 nm was detected by a microplate reader (SpectraMax M4), the cell activity (%) was calculated as (A₀/A_C) × 100.

Western Blotting

Lyse the whole cells in RIPA buffer with 1% (vol/vol) PMSF on ice for 30 min, and then centrifuge the lysates at 12,000 g at 4°C for 10 min. Measure protein concentrations with BCA Protein Assay Kit. The whole cell protein was boiled in SDS loading buffer for 10 min, separated by SDS-PAGE gel and transferred into 0.45nm PVDF membranes. After blocked with 5% skim milk, the PVDF membranes were incubated with HIF1-α and GAPDH antibodies in 4°C overnight. After washing with TBST three times, the PVDF membranes were further incubated with HRP goat anti-mouse IgG at room temperature. Finally, the PVDF membranes were developed by Amersham Imager 600 with ECL reagents.

Cell Death Analysis

4T1 and MCF-7 cells were seeded and cultured in 6-well plates at a density of 2 × 10⁵ cells per well for 24 h and subjected to the indicated treatments. Then the cells were treated with the following conditions under either normoxic or hypoxic conditions: group 1, control; group 2, laser treatment (1.0 W cm⁻²; 5 min); group 3, treatment with 200 µg mL⁻¹ Fe-HCOFs-PEG²⁰⁰⁰; group 4, treatment with 200 µg mL⁻¹ Fe-HCOFs-PEG²⁰⁰⁰ + laser (1.0 W cm⁻²; 5 min) in normoxia; group 5, treatment with 200 µg mL⁻¹ Fe-HCOFs-PEG²⁰⁰⁰ + laser (1.0 W cm⁻²; 5 min) in hypoxia. 12 h later, the cells were washed by PBS twice and then continued to incubate in 37°C for an additional 12 h. Live/Dead cell co-staining and flow cytometry were analyzed by kit instruction (Calcein AM: Ex/Em=494/517 nm, PI: Ex/Em=535/617 nm).

Intracellular ROS Generation

4T1 and MCF-7 cells were seeded and cultured in 12-well plates at a density of 2 × 10⁵ cells per well for 12 h and subjected to the indicated treatments. The concentrations of Fe-HCOFs-PEG²⁰⁰⁰ nanomaterials are 200µg mL⁻¹, and the NIR power is 1.0 W cm⁻²; 5 min. 12 h later, cells were washed with PBS twice and continued to cultivate for 12 h. Fluorescent probe DCFH-DA 10 µM was added and incubated 37°C 20 min after removing the cell culture medium. Cells were washed with PBS twice and taken photos under fluorescence microscope (DCFH-DA: Ex/Em=488/525nm) or collected to be analyzed by flow cytometry.

Intracellular O₂^{•-} Generation

4T1 and MCF-7 cells were seeded and cultured in glass bottom cell culture dishes overnight and subjected to the indicated treatments. The concentrations of Fe-HCOFs-PEG²⁰⁰⁰ nanomaterials are 200µg mL⁻¹, and the NIR power is 1.0 W cm⁻²; 5 min. 12 h later, cells were washed by PBS twice and continued to cultivate for 12 h. Fluorescent probe DHE 10 µM was added and incubated in 37°C 20 min after removing the cell culture medium. Cells washed with PBS twice and were taken photos under Laser Scanning Confocal Microscopy (LSCM) (DHE: Ex/Em=300/610nm).

Mitochondrial Membrane Potential Assay

5 × 10⁴ 4T1 cells were seeded and cultured in glass bottom cell culture dishes overnight and subjected to the indicated treatments. The concentrations of Fe-HCOFs-PEG²⁰⁰⁰ nanomaterials are 200µg mL⁻¹, and the NIR power is 1.0 W cm⁻²; 5 min. 12 h later, cells were washed by PBS twice and continued to cultivate for 12 h. Cells treated with probe JC-1 as kit direction and taken photos under LSCM (JC-1 aggregates: Ex/Em=585/590nm; JC-1 monomers: Ex/Em=514/529 nm).

In vivo Biosafety

Thirty BALB/c mice were randomly divided into 6 groups and treated with different dosages of Fe-HCOFs-PEG²⁰⁰⁰ (0, 5, 10, 20, 30, 40 mg kg⁻¹). Rigorous weight measurements were taken every 2 days for a period of 14 days. Another 15 BALB/c mice were treated with 30 mg kg⁻¹ Fe-HCOFs-PEG²⁰⁰⁰ for 0, 7, or 14 days. Then the blood, heart, liver, spleen lung, and kidney specimen were collected for H&E staining, blood cells classification, and serum biochemistry examination.

In vivo Fluorescence Imaging

Three BALB/c mice were individually administered with 30 mg kg⁻¹ of Fe-HCOFs-PEG²⁰⁰⁰ through tail vein injection. At predetermined time intervals (1, 3, 6, 12, 24, 48, and 72 h), the mice were imaged by IVIS Spectrum.

In vivo PDT

Twenty-four BALB/c mice bearing 4T1 tumors were divided into four groups: PBS, PBS + laser, Fe-HCOFs-PEG²⁰⁰⁰ (30 mg kg⁻¹), Fe-HCOFs-PEG²⁰⁰⁰ (30 mg kg⁻¹) + laser. Mice were injected with different reagents through the tail vein as depicted. After circulation for 24 h, mice were irradiated with 808 nm NIR (1.0 W cm⁻²) laser for 10 min. Seven days later, tumors were dissected, photographed, and executed with HE and IHC assay. The animal experiments were approved by the Animal Protection Committee of Zhengzhou University (No. ZZU-LAC20230331 [04]).

Statistical Method

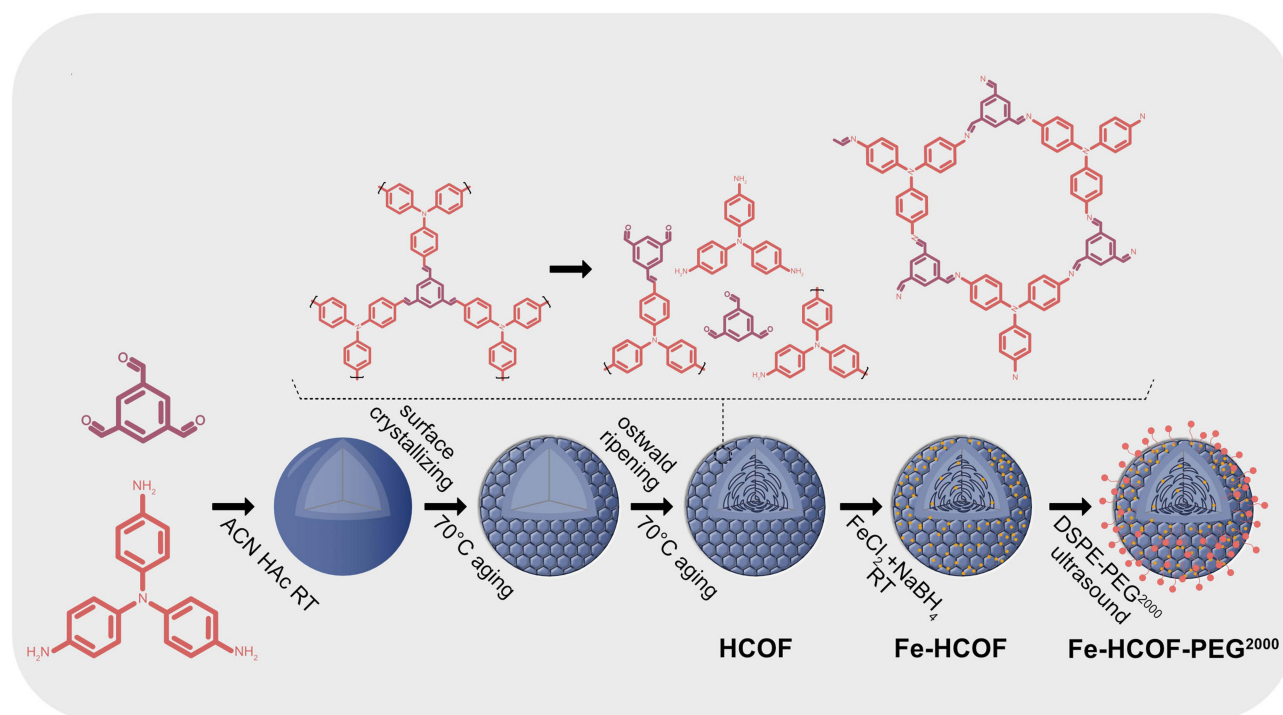
Experimental data were analyzed using GraphPad Prism and Origin software. All experiments were repeated independently at least three times. Comparisons between groups were used *t*-test. *p* < 0.05 was recognized as statistically significant (one-way analysis of variance). **p* < 0.05, ***p* < 0.01, ****p* < 0.001, *****p* < 0.0001. Values are expressed as mean ± SD.

Results

Synthesis and Characterization of Fe-HCOF and Fe-HCOF-PEG²⁰⁰⁰

The details of the synthesis route of Fe-HCOF and Fe-HCOF-PEG²⁰⁰⁰ are shown in [Scheme 1](#). First, covalent organic frameworks (COFs) were synthesized through polymerization of the organic linkers N,N-bis(4-aminophenyl)benzene-1,4-diamine (TAPA) and 1,3,5-benzenetricarbaldehyde (BTCA) in a mixed solution of acetonitrile and glacial acetic acid at room temperature for 6 h to obtain yellow-colored COFs, which were then etched with glacial acetic acid at 70°C for 48 h to prepare hollow COFs (HCOFs).³⁹ Finally, the Fe nanoparticles were loaded onto the HCOFs by reducing ferrous chloride with sodium borohydride in an aqueous solution. The scanning electron microscopy (SEM) images in [Figure 1a](#) illustrate the uniform spherical morphology of the Fe-HCOFs, and the average diameter of the Fe-HCOFs was ~200 nm. Transmission electron microscopy (TEM) images ([Figure 1b](#) and [c](#)) confirmed the formation and flower-like morphology of the Fe-HCOFs, which could be further modified to load drugs. The high-resolution TEM (HRTEM) images in [Figure 1d](#) clearly show ordered lattice fringes, demonstrating the high crystallinity of the HCOFs. The energy dispersive X-ray (EDX) elemental mappings shown in [Figure 1e, f, g, h, and i](#) reveal that C, N, O, and Fe are homogeneously distributed throughout the entire Fe-HCOF structure, indicating the successful synthesis of Fe-HCOFs.

The crystallinity, composition, and porosity of the Fe-HCOFs were further investigated. [Figure 1j](#) shows the Fourier transform infrared (FTIR) spectrum of Fe-HCOFs; an imine bond (C=N) at 1622.30 cm⁻¹ can be clearly observed, demonstrating the successful polymerization of TAPA and BTCA. The characteristic bands of TAPA and BTCA are the aldehydic C-H stretching band (2865.14 cm⁻¹) and the N-H stretching band (3403.15 cm⁻¹). These bands were extremely weak, verifying the disappearance of these two substrates and the formation of HCOFs. X-ray diffraction (XRD) was also conducted to determine the crystallinity of the Fe-HCOFs. As shown in [Figure 1k](#), only two diffraction peaks were observed in the Fe-HCOFs XRD pattern: a sharp peak located at 7.65° and a weak peak located at 13.22°, demonstrating the high crystallinity of the Fe-HCOFs. X-ray photoelectron spectroscopy (XPS) was used to further determine the elemental composition and chemical state, as shown in [Figure S1a–d](#). Fe-HCOFs were shown to consist of abundant C, N, and O and a small quantity of Fe; these results were consistent with the EDX mapping results. The high-



Scheme 1 Schematic illustration of the Fe-HCOF-PEG²⁰⁰⁰ preparation.

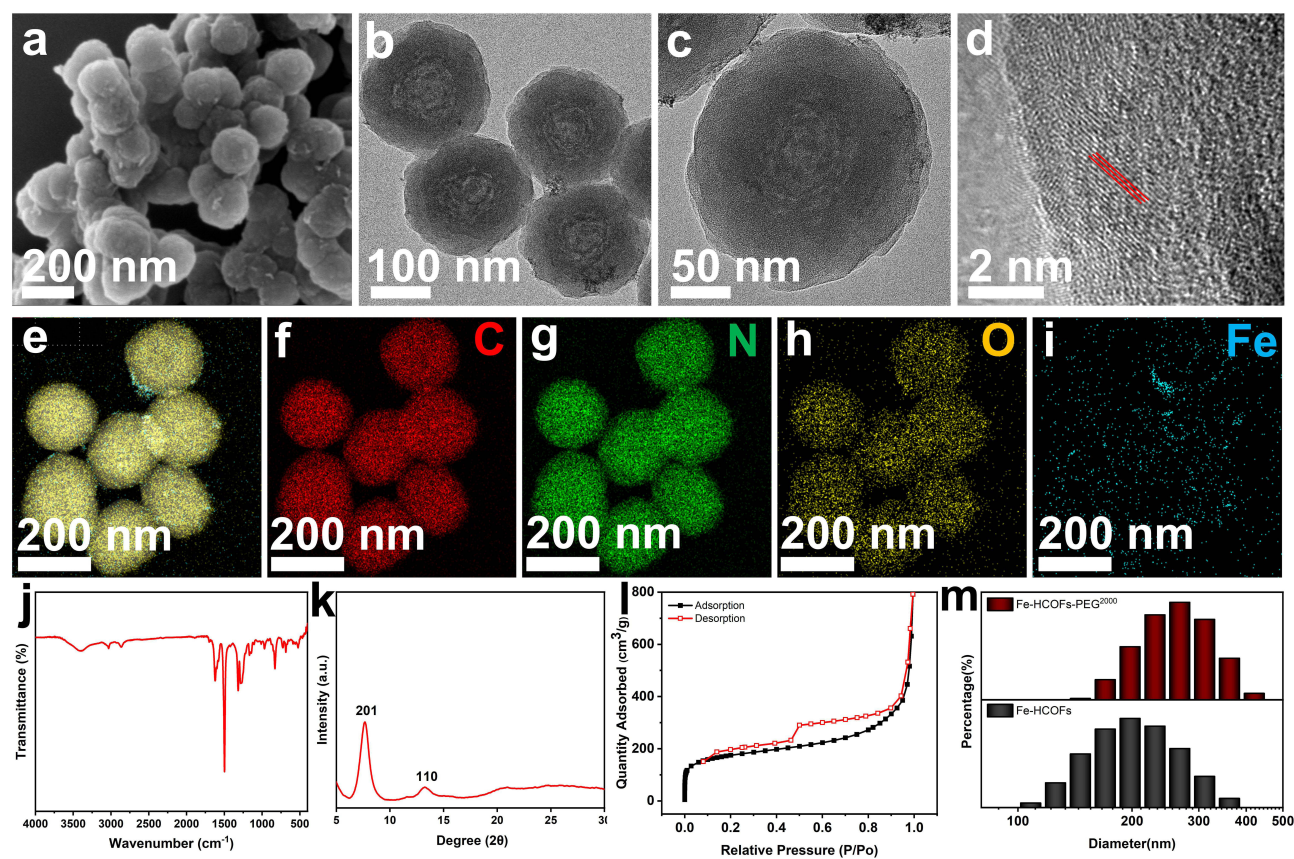


Figure 1 Characterization of Fe-HCOF and Fe-HCOF-PEG²⁰⁰⁰. (a) SEM image of Fe-HCOFs. (b and c) TEM image of Fe-HCOFs. (d) HRTEM image of a part of single Fe-HCOFs nanoparticle. Red line highlighted the ordered lattice fringes. (e) EDS mapping result of Fe-HCOFs for merged elements. (f-i) EDS mapping of C, N, O, and Fe elements in Fe-HCOFs. (j) FTIR transmittable spectrum of Fe-HCOFs. (k) XRD curve of Fe-HCOFs. (l) Nitrogen isothermal adsorption and desorption curves of Fe-HCOFs. (m) Size distribution of Fe-HCOFs and Fe-HCOFs-PEG²⁰⁰⁰ in NaAC buffer.

resolution C 1s, N 1s, and O 1s XPS spectra of the Fe-HCOFs showed that C–C, C=N, and C–O were present in the Fe-HCOFs, which was consistent with the FTIR data. The cumulative pore volume curve (Figure S2) and nitrogen isothermal adsorption and desorption curve (Figure 1l) revealed a type-I sorption isotherm with a rough H3 hysteresis loop, further verifying the microporous nature and irregular pore structure of the Fe-HCOFs.

For the biological application of Fe-HCOFs, the surface was modified with amphiphilic DSPE-PEG2000 to construct Fe-HCOFs-PEG²⁰⁰⁰ with increased stability and circulation time in the physiological environment.⁴⁰ The hydrodynamic size of the Fe-HCOFs-PEG²⁰⁰⁰ was determined through dynamic light scattering (DLS) to be 267.2 nm, which was slightly larger than that of the Fe-HCOFs (197.6 nm) (Figure 1m). The zeta potential of the modified nanomaterial Fe-HCOFs-PEG²⁰⁰⁰ was -21.23 ± 0.76 mV, which had a lower absolute value than that of Fe-HCOFs (-26.2 ± 0.44 mV), indicating greater dispersion in the liquid state (Figure S3).

ROS Generation of Fe-HCOF-PEG²⁰⁰⁰

The ROS formation ability of Fe-HCOFs-PEG²⁰⁰⁰ as an excellent PS was evaluated. 5,5-Dimethyl-1-pyrroline N-oxide (DMPO) was used as a trapping agent to determine the production of $O_2^{\cdot -}$ before and after 808 nm laser illumination in methanol. The electron paramagnetic resonance (EPR) spectra are shown in Figure 2a. A clear signal corresponding to DMPO- $O_2^{\cdot -}$ was observed in the presence of Fe-HCOFs-PEG²⁰⁰⁰ under laser irradiation, whereas no EPR signal was detected in the dark. DMPO could also act as an OH^{\cdot} trapping agent when applied in deionized water. After 10 min of irradiation with an 808 nm laser, the DMPO- OH^{\cdot} signal was also detected in the water system (Figure 2b), indicating high type I photodynamic efficiency. Furthermore, when 2,2,6,6-tetramethylpiperidiny-1-oxide (TEMPO) was used as a 1O_2 -specific probe, the EPR results also showed moderate peaks after irradiation of the Fe-HCOFs-PEG²⁰⁰⁰ (Figure 2c). The mechanism by which Fe-HCOFs-PEG²⁰⁰⁰ generates these ROS is depicted in Figure 2d. Similarly, 2',7'-dichlorodihydrofluorescein (DCFH), which can emit strong fluorescence when oxidized by ROS to 2-dichlorofluorescein (DCF), was used to measure the total ROS. Significant accumulation of fluorescence was observed by measuring the intensity per minute (Figure 2e). The same behavior was observed when exploring the production of $O_2^{\cdot -}$ in the presence of dihydroethidium (DHE) and DNA. The fluorescence curve of the products

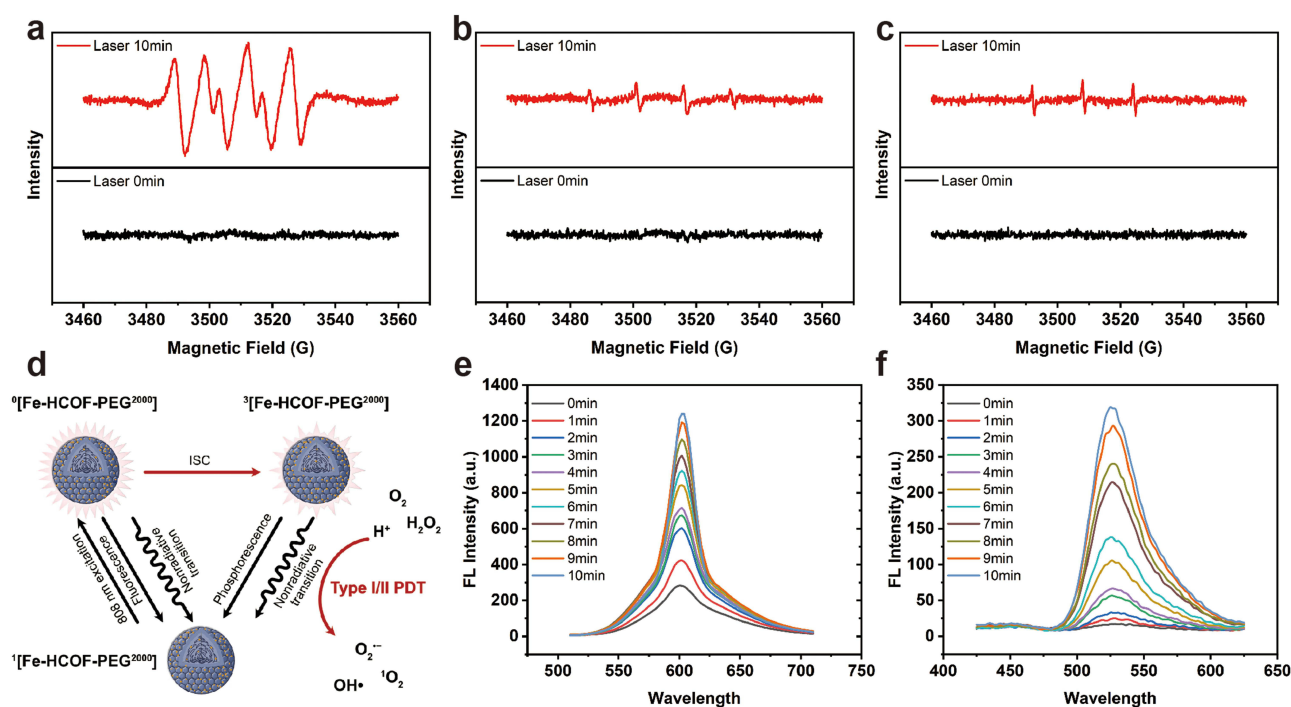


Figure 2 ROS generation of Fe-HCOF-PEG²⁰⁰⁰. The EPR spectrogram of (a) $O_2^{\cdot -}$, (b) OH^{\cdot} and (c) 1O_2 captured by DMPO or TEMPO when they born by Fe-HCOFs under NIR treatment at 10min or 0min time point. (d) Schematic diagram of type I PDT. Fluorescence spectrum of (e) DHE and (f) DCFH-DA motivated by Fe-HCOFs under different duration of 808nm NIR irradiation.

gradually increased and accounted for most of the fluorescence intensity of the ROS, indicating that the Fe-HCOFs-PEG²⁰⁰⁰ excited at 808 nm mainly produced O₂^{•−} rather than other ROS categories (Figure 2f).

Cellular Uptake and Photosensitive Antitumor Effect of Fe-HCOF-PEG²⁰⁰⁰

Since ROS can act only in cells, we first examined whether Fe-HCOFs-PEG²⁰⁰⁰ was internalized by the mouse breast cancer cell line 4T1 and the human breast cancer cell line MCF-7. After incubation with Fe-HCOFs-PEG²⁰⁰⁰ for 24 h or 12 h, a certain increase in the iron concentration was measured in the cytoplasm of 4T1 and MCF-7 cells, as shown in Figure 3a and Figure S4, and the maximum value was reached at 12 h, indicating the best irradiation time.

To further explore the cytotoxicity of Fe-HCOFs-PEG²⁰⁰⁰ in vitro, we carried out a CCK-8 assay to assess the viability of 4T1 and MCF-7 cells. As shown in Figure 3b and c, Fe-HCOFs-PEG²⁰⁰⁰ showed little cytotoxicity in the absence of light until the concentration reached 200 µg mL^{−1}. Once 808 nm NIR was applied, the mortality rate raised with increasing concentrations of Fe-HCOFs-PEG²⁰⁰⁰ and eventually reached approximately 70%, even in a hypoxic atmosphere. The protein level of HIF1-α, a hypoxia-specific biomarker that was distinctly upregulated in the hypoxia group, was measured to confirm the presence of normoxic or hypoxic conditions (Figure 3d and e, Figure S5a and b). The live/dead co-staining assay (Figure 3f and Figure S6) was another pivotal method for verifying the photocytotoxicity of Fe-HCOFs-PEG²⁰⁰⁰. Consistent with the results of the CCK-8 assay, most of the stained cells in the sample died after treatment with 200 µg mL^{−1} Fe-HCOFs-PEG²⁰⁰⁰ plus irradiation under both normoxic and hypoxic conditions. Cell viability was assessed by flow cytometry (Figure 3g and Figure S7), and the results showed that when the concentration of Fe-HCOFs-PEG²⁰⁰⁰ was 100 µg mL^{−1} and the 808 nm NIR intensity was 1.0 W cm^{−2}, the cell mortality rates were similar under normoxic and hypoxic conditions, whereas minimal damage was observed when the cells were treated only with either Fe-HCOFs-PEG²⁰⁰⁰ or a laser. Notably, compared with those in the NC group, the side scatter (SSC) of cells in the Fe-HCOFs-PEG²⁰⁰⁰-treated group was increased, but no significant difference in cell viability was observed via flow cytometry, further indicating the cellular uptake of Fe-HCOFs-PEG²⁰⁰⁰.

Since 808 nm NIR light is commonly used in photothermal therapy,^{41–43} we hypothesized that Fe-HCOFs-PEG²⁰⁰⁰ would exert a photothermal effect under 808 nm NIR irradiation. However, no evident difference was observed in the mortality of 4T1 or MCF-7 cells exposed to 808 nm NIR light at room temperature or on ice (Figure S8a and b). These results indicated that Fe-HCOFs-PEG²⁰⁰⁰-induced cell death could be due to overproduction of intracellular ROS. Notably, after 100 µM vitamin C was added to the cells incubated with Fe-HCOFs-PEG²⁰⁰⁰, the photogenicity was not as intense as before after 808 nm laser irradiation (Figure S8c and d). Therefore, the effect of Fe-HCOFs-PEG²⁰⁰⁰ was achieved through a photodynamic effect rather than a photothermal effect.

Anticancer Mechanism of Fe-HCOF-PEG²⁰⁰⁰

Intracellular ROS generation contributes to multiple types of damage, including DNA, RNA, proteins, and important organelles, ultimately leading to cancer cell death.⁴⁴ Inspired by ROS production by Fe-HCOFs-PEG²⁰⁰⁰, we decided to determine whether Fe-HCOFs-PEG²⁰⁰⁰ maintained their photodynamic characteristics in cancer cells. Therefore, we investigated the cytotoxic effects attributed to ROS release and the ferroptotic effects attributed to nanoabsorption when cellular internalized Fe-HCOFs-PEG²⁰⁰⁰ were irradiated with NIR light under normoxic or hypoxic conditions. As illustrated in Figure 4a and c and Figures S9 and S10, we used DCFH-DA as an ROS detection probe in cells. The fluorescence intensity increased markedly when the cells were treated with Fe-HCOFs-PEG²⁰⁰⁰ and irradiated at 808 nm, whereas cells treated with only Fe-HCOFs-PEG²⁰⁰⁰ or the laser emitted negligible amounts of green signal. Flow cytometry (Figure 4b, Figure S11) showed identical results; flat ROS-positive 4T1 cell peaks were observed in the control, Fe-HCOFs-PEG²⁰⁰⁰-only and laser-only groups, while a large increase in the number of ROS-positive cells appeared after combination treatment with Fe-HCOFs-PEG²⁰⁰⁰ and laser irradiation. Similar results were observed in the MCF-7 cell line. DHE is a commonly used O₂^{•−} fluorescence detection probe for living cells that can react with intracellular O₂^{•−} to produce red fluorescence. 4T1 cells treated with Fe-HCOFs-PEG²⁰⁰⁰ and NIR light presented strong red fluorescence even at low oxygen concentrations, indicating that Fe-HCOFs-PEG²⁰⁰⁰ had excellent O₂^{•−}-generation specificity under light stimulation (Figure 4d and e, Figures S12 and S13). Overall, the above results confirmed that with

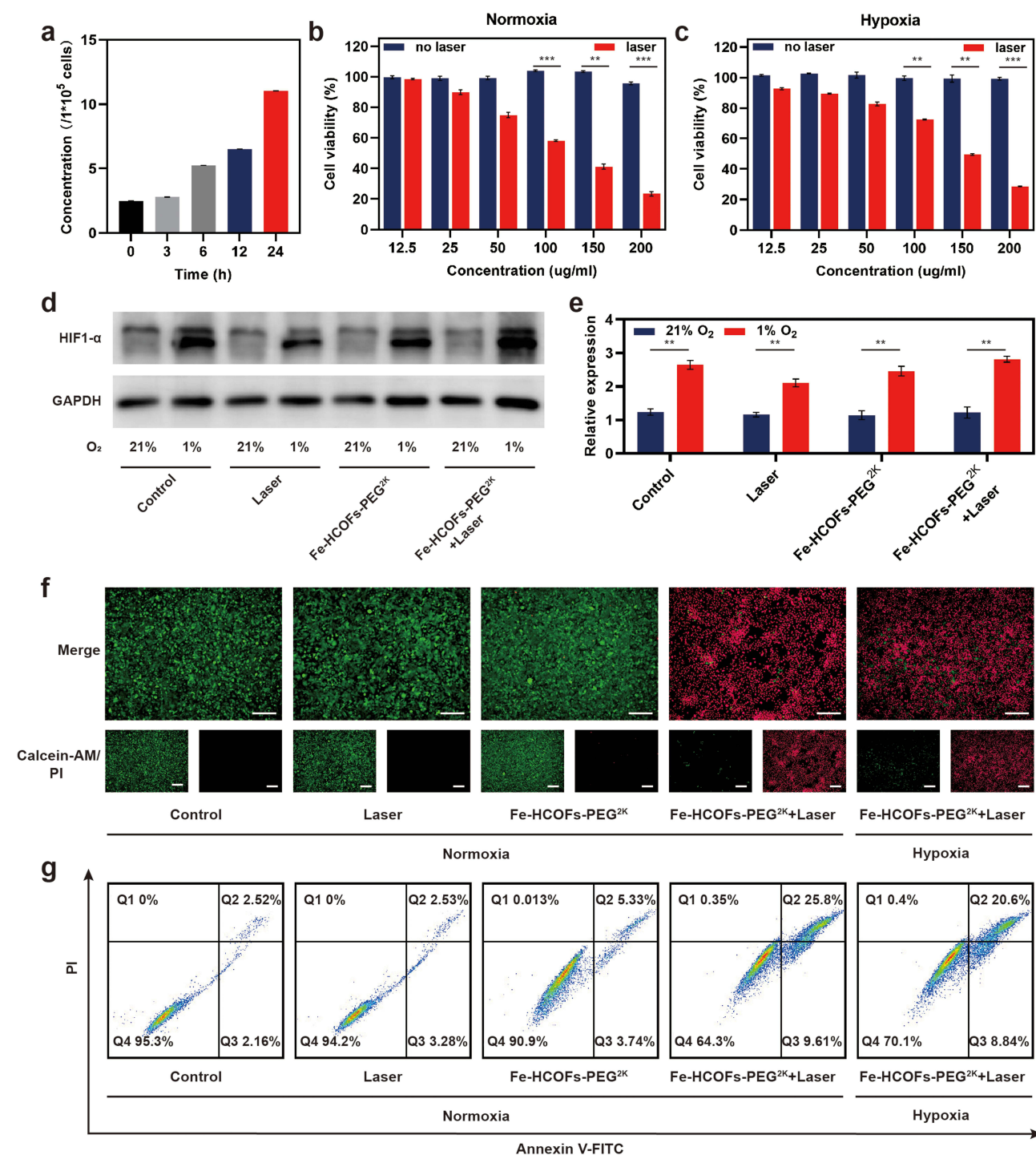


Figure 3 Cell absorption and photosensitive antitumor effect of Fe-HCOF-PEG²⁰⁰⁰. (a) Cellular uptake of Fe-HCOFs in 4T1 cells detected by ICP-MS. n=3. The relative viabilities of 4T1 cells incubated in different Fe-HCOFs concentrations with or without NIR irradiation in (b) normoxia and (c) hypoxia. n=3. Data are shown as mean ± SD. Student's t-test, **p < 0.01, ***p < 0.001. (d) WB analysis and (e) relative expression of HIF-1α in 4T1 cells treated with or without Fe-HCOFs-PEG²⁰⁰⁰ and laser in different O₂ atmospheres. n=3. Data are shown as mean ± SD. Student's t-test, **p < 0.01. (f) Fluorescence images of Fe-HCOFs-PEG²⁰⁰⁰ and laser treated or not treated 4T1 cells stained by Calcein-AM/PI under normoxia and hypoxia. Scale bar: 100 μm. (g) Flow cytometry assays of 4T1 cells stained by Annexin V-FITC/PI at illustrated therapeutic modalities.

the endocytosis of Fe-HCOFs-PEG²⁰⁰⁰ plus laser irradiation, very large amounts of ROS were produced in the cells even in a hypoxic atmosphere, and the ROS-induced cytotoxicity in solid and hypoxic tumor tissues.

Ferroptosis, occurs after ROS accumulation and lipid peroxidation caused by iron metabolism, has frequently been reported in nano-mediated cell death in recent years. Fe-HCOFs-PEG²⁰⁰⁰-loaded Fe²⁺ and light-triggered ROS are

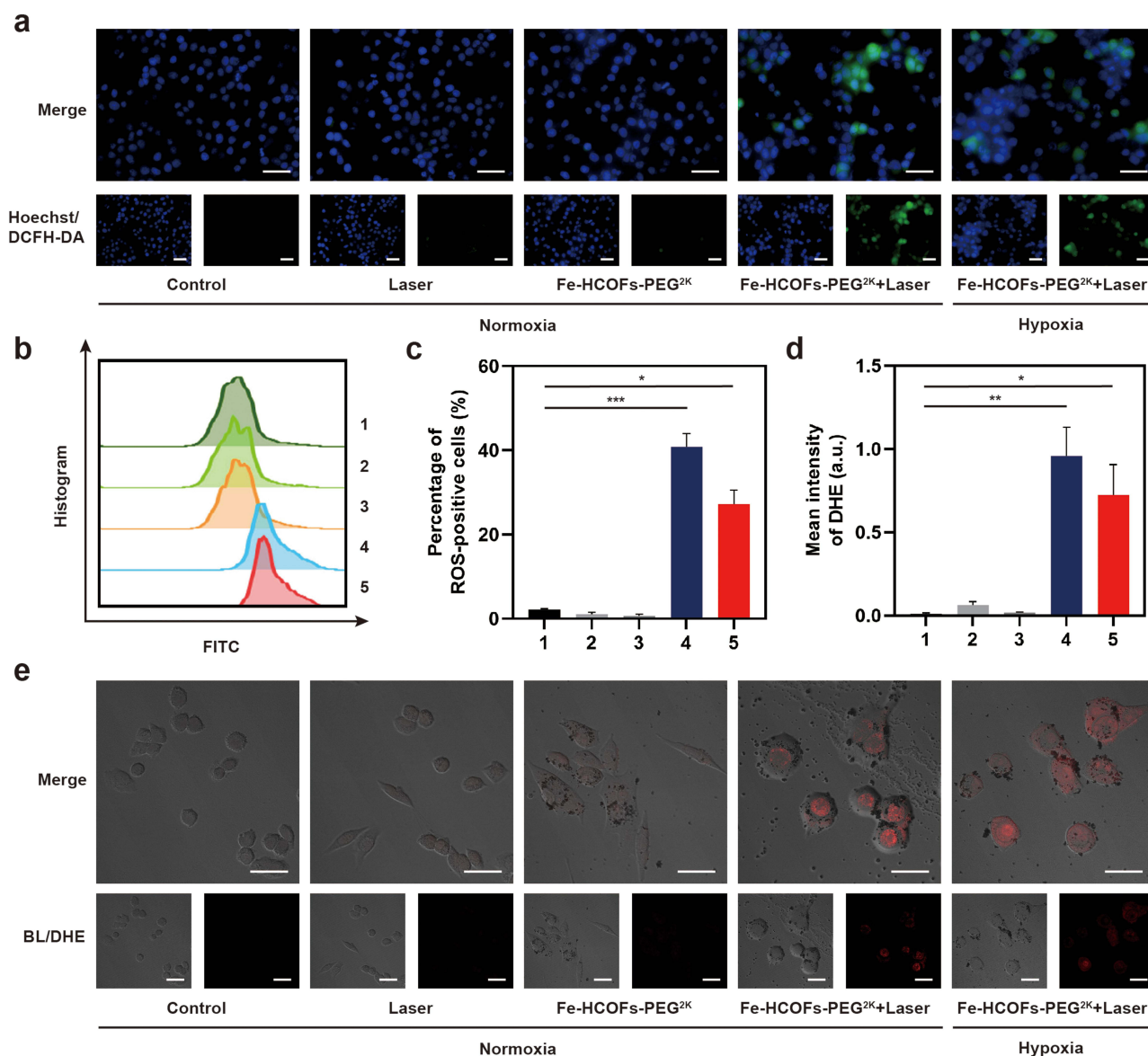


Figure 4 ROS production of Fe-HCOF-PEG²⁰⁰⁰ in cancer cells. (a) Fluorescence images of DCFH-DA probe bonded 4T1 cells to detect cellular ROS generation. Scale bar: 50 μ m. (b) Flow cytometry of DCFH-DA probe bonded 4T1 cells to detect cellular ROS generation. (c and d) Quantitative intensity of DCFH-DA in Figure a and DHE in Figure e, respectively. n=3. Data are shown as mean \pm SD. Student's t-test, * p < 0.05, ** p < 0.01, *** p < 0.001. (e) DHE staining images of 4T1 cells treated with 5 definite methods to indicate $O_2^{\cdot-}$ positive cells. Scale bar: 20 μ m.

important inducing factors of ferroptosis; therefore, we wondered whether Fe-HCOFs-PEG²⁰⁰⁰-catalyzed cell death was partly attributable to ferroptosis and examined this possibility in 4T1 cells. We compared the results of transcriptome sequencing analyses of the control (group 1) and Fe-HCOFs-PEG²⁰⁰⁰-treated groups under hypoxia (group 2), which were verified by the upregulation of HIF1 signaling pathway in the KEGG enrichment scatter. We also found significant changes in glutathione metabolism and apoptosis, indicating Fe-HCOFs-PEG²⁰⁰⁰ potentially induced ferroptosis (Figure 5a). Moreover, the expression of ferroptosis markers obtained from the FerrDb V2 (<http://www.zhounan.org/ferrdb/current/>) were nearly opposite to each other according to the heatmap (Figure 5b). A variety of important regulatory molecules, such as SLC7A11, GPX4, and ACSL4, play key roles in regulating ferroptosis. Western blot (WB) analysis revealed that these parameters clearly changed in the laser-irradiated Fe-HCOFs-PEG²⁰⁰⁰ treatment groups (Figure 5c). Excessive ROS trigger oxidative stress and lipid peroxidation in cells, which eventually decompose into a series of complex compounds, including malondialdehyde (MDA).⁴⁵ MDA can react with thiobarbituric (TBA) to

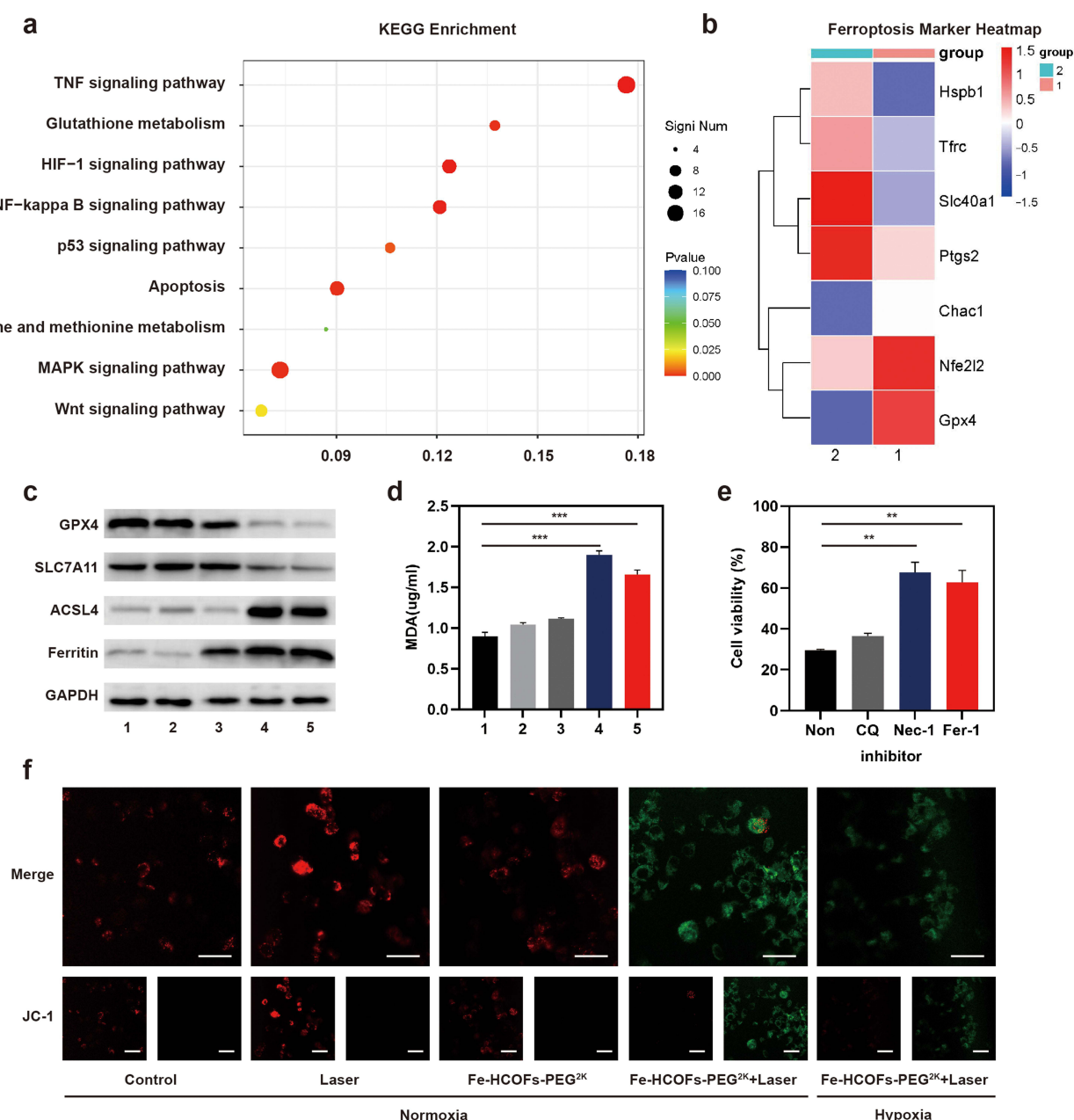


Figure 5 Fe-HCOF-PEG²⁰⁰⁰ induced ferroptosis in cancer cells. (a) KEGG enrichment scatter of group2 (Fe-HCOFs-PEG²⁰⁰⁰+laser in hypoxia) vs group1 (control). n=3. (b) Ferroptosis marker heatmap of group 2 and group 1. n=3. (c) WB analysis of ferroptosis markers (ACSL4, GPX4, SLC7A11) and Ferritin in 4T1 cells. (d) MDA concentration of 4T1 cells treated with 5 definite methods. n=3. Data are shown as mean \pm SD. Student's t-test, *** p < 0.001. (e) Cell viability of 4T1 cells treated by 200ug/mL Fe-HCOFs-PEG²⁰⁰⁰ and laser, then rescued by 3 different PCD inhibitors (CQ, Nec-1, Fer-1). n=3. Data are shown as mean \pm SD. Student's t-test, ** p < 0.01. (f) Mitochondrial membrane potential of 4T1 cells marked by JC-1 probe under 5 certain treatments. Scale bar: 20 μ m.

form a red adduct with a maximum absorption peak at 535 nm. The 535 nm absorbance in Fe-HCOFs-PEG²⁰⁰⁰ + laser irradiation-treated 4T1 cells showed a significant increase compared with NC group whether in normoxia or hypoxia, indicating Fe-HCOFs-PEG²⁰⁰⁰ had photo-capable MDA production ability at any oxygen concentration (Figure 5d). Surprisingly, Fe-HCOFs-PEG²⁰⁰⁰ can induce ferroptosis even in a hypoxic environment, at similar levels to those under normoxic conditions. After laser-activated Fe-HCOFs-PEG²⁰⁰⁰ treatment, ferroptosis-related death was reduced to some extent by the ferroptosis inhibitor Fer-1 and the necroptosis inhibitor Nec-1, further verifying the mode of ferroptosis-related cell death (Figure 5e). Moreover, we showed that Fe-HCOFs-PEG²⁰⁰⁰ with laser irradiation triggers alterations in mitochondrial membrane potential (MMP) via JC-1, which results in a red or green fluorescent signal in cells that defines

normal or impaired mitochondria. As illustrated in Figure 5f, intense green fluorescence with 490 nm light excitation was monitored in the Fe-HCOFs-PEG²⁰⁰⁰ and laser treatment groups under 21% O₂ and 2% O₂, and only red fluorescence was detected in the Fe-HCOFs-PEG²⁰⁰⁰-only or laser treatment-only groups.

In vivo Evaluation of the Biocompatibility and Biodistribution

Since the biocompatibility of Fe-HCOFs-PEG²⁰⁰⁰ needed to be demonstrated in vivo, we injected Fe-HCOFs-PEG²⁰⁰⁰ into BALB/c mice via the tail vein to confirm that the presence of Fe-HCOFs-PEG²⁰⁰⁰ was harmless when the cells were in circulation. As shown in Figure S14, mouse body weight increased slightly and did not differ significantly among the different Fe-HCOFs-PEG²⁰⁰⁰ doses (0, 5, 10, 20, 30, and 40 mg kg⁻¹). The major organs and blood of 30 mg kg⁻¹ Fe-HCOFs-PEG²⁰⁰⁰-treated mice were collected after 7 and 14 days to examine the morphology and physiological indices via hematoxylin and eosin (H&E) staining (Figure 6a), serum biochemistry examination (Figure 6b) and blood cell classification (Figure 6c). The results showed no apparent histopathological, circulation, or liver or kidney function abnormalities, indicating the excellent biocompatibility of Fe-HCOFs-PEG²⁰⁰⁰.

Since Fe-HCOFs have remarkable internalization efficiency in tumor cells, we determined whether they could feasibly target tumors in vivo. We used Cy5.5-labeled Fe-HCOFs-PEG²⁰⁰⁰ (30 mg kg⁻¹) to detect biodistribution in 4T1 tumor-bearing BALB/c mice (Figure 6d). Over time, the Cy5.5 fluorescence spot accumulated in the tumor and reached a maximum at 24 h after Fe-HCOFs-PEG²⁰⁰⁰ injection. Notably, the fluorescence intensity remained high even 72 h after injection, probably due to the enhanced permeability and retention (EPR) effect.⁴⁶ We also collected visceral samples 24 h after nanoparticle usage, as shown in Figure 6e. Fe-HCOFs-PEG²⁰⁰⁰ are effectively aggregated in tumors, with relatively high concentrations only in the liver and kidney, which are responsible for biotransformation and metabolism. These results confirmed the biosafety and accumulation of Fe-HCOFs-PEG²⁰⁰⁰ when used as anti-tumor nanomedicine.

In vivo Verification of Antitumor Ability

To further investigate the synergistic photodynamic therapeutic efficacy of Fe-HCOFs-PEG²⁰⁰⁰ in vivo, 24 BALB/c mice bearing 4T1 tumors were divided into four groups and treated as described above: PBS, PBS + laser, Fe-HCOFs-PEG²⁰⁰⁰ (30 mg kg⁻¹), and Fe-HCOFs-PEG²⁰⁰⁰ (30 mg kg⁻¹) + laser. To maximize the synergistic effect of phototherapy, 24 h was selected as the laser therapeutic time based on the results of the distribution assay. Then, we measured the body weights and tumor sizes every 2 days and collected the tumors at the end of the experiment. Figure 7a and b show the final tumor images and weights of the four different therapy groups. Fe-HCOFs-PEG²⁰⁰⁰ (30 mg kg⁻¹)+laser therapy significantly inhibited tumor growth in mice. The same trend was observed for tumor size, as shown in Figure 7c. After treatment, we collected the tumors and performed immunofluorescence staining (IF) for GPX4, an important inhibitory biomarker of ferroptosis.²⁷ In accordance with the in vitro results, the lowest expression level of GPX4 was observed in the Fe-HCOFs-PEG²⁰⁰⁰ (30 mg kg⁻¹)+laser group (Figure 7d). H&E staining, immunohistochemistry (IHC) of TUNEL, and IF of HIF1- α were also used to detect tumor cell apoptosis under hypoxia. The Fe-HCOFs-PEG²⁰⁰⁰ (30 mg kg⁻¹)+laser-treated mouse tumor slices presented the reddest colloid without cellular structure or TUNEL-positive cells, indicating the outstanding tumor-killing effect of the Fe-HCOFs-PEG²⁰⁰⁰ under NIR irradiation even in hypoxic tumor microenvironment (Figures 7e). These results successfully confirmed that Fe-HCOFs-PEG²⁰⁰⁰ promoted ferroptosis and inhibited tumor growth in vivo.

Discussion and Conclusion

In summary, we developed highly active and less oxygen-dependent photodynamic nanomedicine in the field of tumor therapy. Fe-HCOFs-PEG²⁰⁰⁰ generate different types of ROS, especially O₂⁻, to induce tumor cell death under 808 nm NIR laser irradiation. Based on the porous structure of the HCOF nanomaterials, we loaded Fe nanoparticles on them to increase their cytotoxicity in cooperation with ROS generation after uptake into the cytoplasm. The fundamental mechanism underlying the lethality of Fe-HCOF-PEG²⁰⁰⁰ under laser irradiation was clarified via cell-based experiments and transcriptome sequencing. Fe-HCOF-PEG²⁰⁰⁰ first entered the cytoplasm and produced ROS, leading to cell

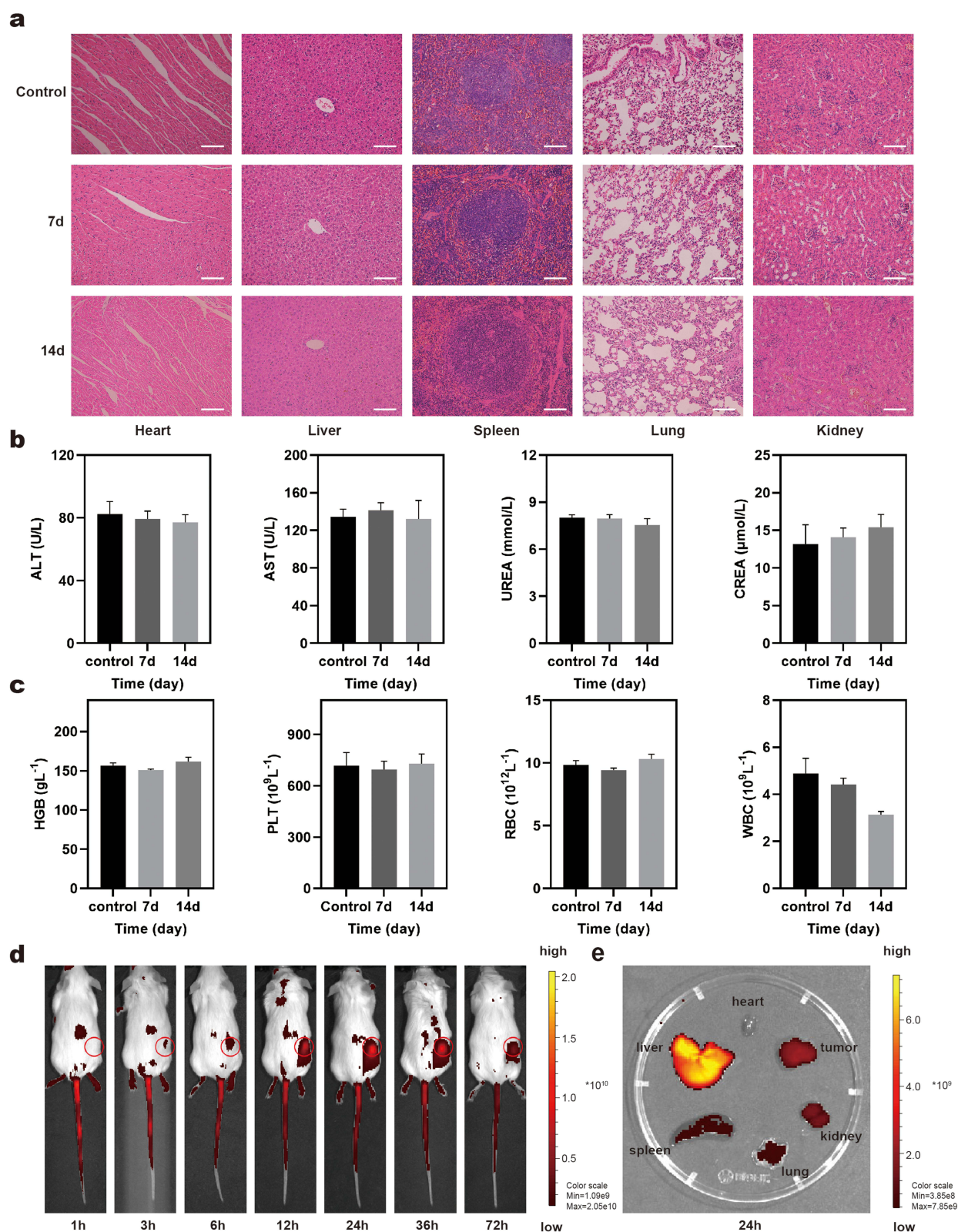


Figure 6 In vivo biocompatibility of Fe-HCOF-PEG²⁰⁰⁰. (a) H&E staining of 30 mg kg⁻¹ Fe-HCOFs-PEG²⁰⁰⁰ dosage treated BALB/c mice at 7 and 14 days. n=5. Scale bar: 100 μm. (b) ALT, AST, UREA and CREA content in 30 mg kg⁻¹ Fe-HCOFs-PEG²⁰⁰⁰ dosage treated BALB/c mice serum. n=3. (c) HGB, PLT, RBC and WBC content in 30 mg kg⁻¹ Fe-HCOFs-PEG²⁰⁰⁰ dosage treated BALB/c mice blood. n=3 (d) Fe-HCOFs-PEG²⁰⁰⁰ distribution of 4T1 tumor-bearing mice by IVIS. Tumors are marked with red circles. (e) Fe-HCOFs-PEG²⁰⁰⁰ enrichment in main organ and tumor after 72h injection.

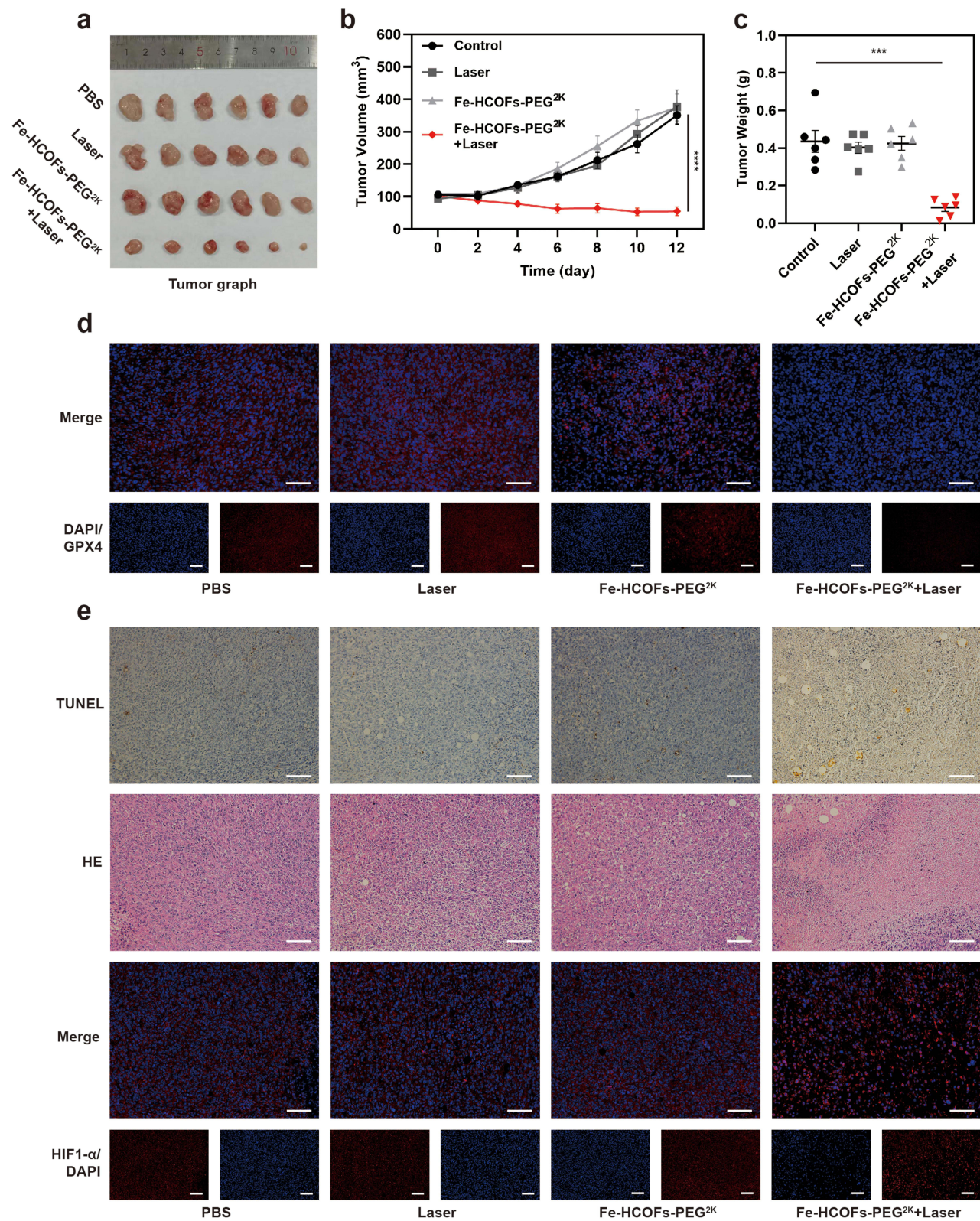


Figure 7 In vivo biodistribution and antitumor ability of Fe-HCOF-PEG²⁰⁰⁰. (a) Tumor graph, (b) volume and (c) weight in 4 groups: PBS, PBS + Laser, Fe-HCOFs-PEG²⁰⁰⁰, Fe-HCOFs-PEG²⁰⁰⁰ + Laser. n=6. Data are shown as mean ± SD. Student's t-test, ***p < 0.001, ****p < 0.0001. (d) Immunofluorescence image for GPX4 and DAPI, (e) Immunohistochemistry image of tumor tissue, H&E staining of tumor tissue and Immunofluorescence image for HIF1-α and DAPI in 4 groups: PBS, PBS + Laser, Fe-HCOFs-PEG²⁰⁰⁰, Fe-HCOFs-PEG²⁰⁰⁰ + Laser. Scale bar: 100 μm.

apoptosis; moreover, the nano-induced ion disturbance and lipid peroxidation led to ferroptosis. Ultimately, *in vivo* experiments on biosafety, tumor targeting, and antitumor ability in mouse models confirmed that Fe-HCOF-PEG²⁰⁰⁰ has potential as an innovative type I&II PDT drug.

The design of phototheranostic agents and exploration of potential biomechanisms have recently attracted considerable research attention from the materials and medical fields. We created Fe-HCOF-PEG²⁰⁰⁰ as a superior type I&II PS that depends on the semiconducting polymer (SP) essence and porous structure. Efficient electron transfer can occur under light-harvesting conditions.^{47,48} However, SPs and structural editing only enhance the limited PDT efficiency, and the potential molecular structure of Fe-HCOF-PEG²⁰⁰⁰ designed for promoting intersystem crossing (ISC) processes and energy utilization is urgent to explore.⁴⁹ An increasing number of studies have introduced COF materials loaded with PSs and ferroptosis inducers to trigger ROS generation and ferroptosis in cancer therapy.^{50–53} Most of them regard COFs as nanocarriers and ignore the hypoxic tumor environment. We propose the use of Fe-HCOF-PEG²⁰⁰⁰ to complement hypoxic solutions in combination with ferroptotic cancer therapy. More biomarkers of ferroptosis were detected in Fe-HCOF-PEG²⁰⁰⁰ induced cell death. Regrettably, ferroptosis can be detected under normoxia and hypoxia, and whether the hypoxic environment inhibits ferroptosis and the detailed molecular mechanisms induced by Fe-HCOF-PEG²⁰⁰⁰ need to be further investigated.

Clinical translation of COF-based nanomedicine has presented lasting challenges and perspectives, including biosafety, pharmacokinetics, potential immune responses, large-scale synthesis, and scalability of the synthesis process. COFs have exhibited significant biosafety in preclinical research since their first use in cancer therapy. As a type of COF, Fe-HCOF-PEG²⁰⁰⁰ showed excellent biocompatibility even when the concentration reached 200 $\mu\text{g mL}^{-1}$ *in vitro* and 40 mg kg^{-1} *in vivo*. Limitedly, the cells were incubated with Fe-HCOF-PEG²⁰⁰⁰ for only 24 hours, and the BALB/c mice were injected with Fe-HCOF-PEG²⁰⁰⁰ for only 14 days. The long-term toxic effects were obscure in our present research. Moreover, we did not detect the pharmacokinetic profile of Fe-HCOF-PEG²⁰⁰⁰ because of the natural presence of iron in the mouse body. The metabolism of Fe-HCOF-PEG²⁰⁰⁰ is unpredictable. Many studies have demonstrated the immunotherapy efficiency of COF nanomaterials. They can deliver immunogenic cell death (ICD) inert monomers, remodel the tumor microenvironment to trigger antitumor immunity and increase immunogenic programmed cell death.^{51,54,55} Interestingly, transcriptome sequencing revealed that activated Fe-HCOF-PEG²⁰⁰⁰ can trigger the TNF signaling pathway and NF- κ B signaling pathway in 4T1 cells. TNF activates TNF receptors, recruits adaptor proteins, and then triggers cascade reactions of related pathways, including the NF- κ B pathway, to regulate inflammation, cell death, or cell survival.⁵⁶ Notably, ROS are important inducers of the TNF signaling pathway,⁵⁷ and Fe-HCOF-PEG²⁰⁰⁰ probably has no influence on immune responses without NIR stimulation. However, whether photodynamic and ferroptosis induce an inflammatory response to inhibit tumor growth and metastasis is worth research. Commercial scale production is emerging as an important goal in clinical usage of nanomedicine. Fe-HCOF-PEG²⁰⁰⁰ have finished the transformation of amorphous-to-crystalline, stable and uniform morphologies have characterized in Figure 1. Additionally, Fe-HCOF-PEG²⁰⁰⁰ was not modified with the biological components, such as cell membrane, antigens, and nucleic acids. This indicates economic and convenient storage. However, the synthesis process of Fe-HCOF-PEG²⁰⁰⁰ needs to be precise and controllable, and intelligent instruments should be equipped for large-scale synthesis. Excitingly, the particle size of Fe-HCOF-PEG²⁰⁰⁰ could be controlled by using different amounts of HAc, and the organic linkages could be changed by replacing monomers under similar conditions.³⁹ The amount of Fe loading can also be artificially assessed for patients in different states. In summary, the scalability of Fe-HCOF-PEG²⁰⁰⁰ inspires various clinical translations.

This research not only provides an additional photodynamic COF but also broadens the application of ferroptosis in tumor inhibition, which will provide new insights for developing PSs and cancer therapy.

Data Sharing Statement

The data that support the findings of this study are available in the Supporting Information of this article.

Ethics Approval and Informed Consent

The animal experiments were approved by the Animal Protection Committee of Zhengzhou University (No. ZZU-LAC20230331 [04]). The welfare of laboratory animals followed Laboratory animals—General code of animal welfare (GB/T 42011-2022).

Acknowledgments

The authors acknowledge the financial support from National Natural Science Foundation of China (81874188); Outstanding Youth Foundation of Henan Province (222300420071); Fund for Distinguished Young Scholars of medical science and technology innovation in Henan Province (YXKC2022033); Fund for Scientific Research and Innovation Team of The First Affiliated Hospital of Zhengzhou University (QNCXTD2023018); Postdoctoral Science Foundation of China (2022T150554); Postdoctoral Science Foundation of Henan Province (202102079).

Disclosure

The authors declare no conflict of interest.

References

- Ding L, Lin X, Lin Z, et al. Cancer cell-targeted photosensitizer and therapeutic protein co-delivery nanoplatform based on a metal-organic framework for enhanced synergistic photodynamic and protein therapy. *ACS Appl Mater Interfaces*. 2020;12(33):36906–36916. doi:10.1021/acsami.0c09657
- Dolmans DE, Fukumura D, Jain RK. Photodynamic therapy for cancer. *Nat Rev Cancer*. 2003;3(5):380–387. doi:10.1038/nrc1071
- Lan M, Zhao S, Liu W, Lee CS, Zhang W, Wang P. Photosensitizers for photodynamic therapy. *Advanced Healthcare Materials*. 2019;8(13):e1900132. doi:10.1002/adhm.201900132
- Sun Y, Zhao D, Wang G, et al. Recent progress of hypoxia-modulated multifunctional nanomedicines to enhance photodynamic therapy: opportunities, challenges, and future development. *Acta pharmaceutica Sinica B*. 2020;10(8):1382–1396. doi:10.1016/j.apsb.2020.01.004
- Wan Y, Fu LH, Li C, Lin J, Huang P. Conquering the hypoxia limitation for photodynamic therapy. *Adv Mater*. 2021;33(48):e2103978. doi:10.1002/adma.202103978
- Chen D, Xu Q, Wang W, Shao J, Huang W, Dong X. Type I photosensitizers revitalizing photodynamic oncotherapy. *Small*. 2021;17(31):e2006742. doi:10.1002/sml.202006742
- Zhao X, Pachfule P, Thomas A. Covalent organic frameworks (COFs) for electrochemical applications. *Chem Soc Rev*. 2021;50(12):6871–6913. doi:10.1039/D0CS01569E
- Wang Z, Zhang S, Chen Y, Zhang Z, Ma S. Covalent organic frameworks for separation applications. *Chem Soc Rev*. 2020;49(3):708–735. doi:10.1039/C9CS00827F
- Meng Z, Mirica KA. Covalent organic frameworks as multifunctional materials for chemical detection. *Chem Soc Rev*. 2021;50(24):13498–13558. doi:10.1039/d1cs00600b
- Ma J, Shu T, Sun Y, et al. Luminescent covalent organic frameworks for biosensing and bioimaging applications. *Small*. 2022;18(3):e2103516. doi:10.1002/sml.202103516
- Esrafil A, Wagner A, Inamdar S, Acharya AP. Covalent organic frameworks for biomedical applications. *Adv Healthcare Mater*. 2021;10(6):e2002090. doi:10.1002/adhm.202002090
- Khan N, Slathia G, Kaliya K, Saneja A. Recent progress in covalent organic frameworks for cancer therapy. *Drug Discovery Today*. 2023;28(6):103602. doi:10.1016/j.drudis.2023.103602
- Yao S, Liu Z, Li L. Recent progress in nanoscale covalent organic frameworks for cancer diagnosis and therapy. *Nano-Micro Lett*. 2021;13(1):176. doi:10.1007/s40820-021-00696-2
- Waller PJ, Gándara F, Yaghi OM. Chemistry of covalent organic frameworks. *Acc Chem Res*. 2015;48(12):3053–3063. doi:10.1021/acs.accounts.5b00369
- Shi YA-O, Yang J, Gao FA-O, Zhang QA-O. Covalent organic frameworks: recent progress biomedicine application. *ACS Nano*. 2023;17(3):1879–1905.
- Wang L, Xie H, Lin Y, et al. Covalent organic frameworks (COFs)-based biosensors for the assay of disease biomarkers with clinical applications. *Biosens Bioelectron*. 2022;217:114668. doi:10.1016/j.bios.2022.114668
- Geng K, He T, Liu R, et al. Covalent organic frameworks: design, synthesis, and functions. *Chem Rev*. 2020;120(16):8814–8933. doi:10.1021/acs.chemrev.9b00550
- Guan Q, Zhou LL, Lv FH, Li WY, Li YA, Dong YB. A glycosylated covalent organic framework equipped with BODIPY and CaCO₃ for synergistic tumor therapy. *Angewandte Chemie*. 2020;59(41):18042–18047. doi:10.1002/anie.202008055
- Wang SB, Chen ZX, Gao F, et al. Remodeling extracellular matrix based on functional covalent organic framework to enhance tumor photodynamic therapy. *Biomaterials*. 2020;234:119772. doi:10.1016/j.biomaterials.2020.119772
- Zhang C, Guo J, Zou X, et al. Acridine-based covalent organic framework photosensitizer with broad-spectrum light absorption for antibacterial photocatalytic therapy. *Adv Healthcare Mater*. 2021;10(19):e2100775. doi:10.1002/adhm.202100775
- Yao S, Zhao X, Wan X, et al. π - π conjugation promoted nanocatalysis for cancer therapy based on a covalent organic framework. *Mater Horizons*. 2021;8(12):3457–3467. doi:10.1039/D1MH01273H
- Sun D, Chen J, Wang Y, et al. Advances in refunctionalization of erythrocyte-based nanomedicine for enhancing cancer-targeted drug delivery. *Theranostics*. 2019;9(23):6885–6900. doi:10.7150/thno.36510
- Zhu L, Zhong Y, Wu S, et al. Cell membrane camouflaged biomimetic nanoparticles: focusing on tumor theranostics. *Materials Today Bio*. 2022;14:100228. doi:10.1016/j.mtbio.2022.100228
- Agostinis P, Berg K, Cengel KA, et al. Photodynamic therapy of cancer: an update. *Ca a Cancer J Clin*. 2011;61(4):250–281. doi:10.3322/caac.20114
- Gao W, Wang X, Zhou Y, Wang X, Yu Y. Autophagy, ferroptosis, pyroptosis, and necroptosis in tumor immunotherapy. *Signal Transduction Target Therapy*. 2022;7(1):196. doi:10.1038/s41392-022-01046-3

26. Chen X, Kang R, Kroemer G, Tang D. Broadening horizons: the role of ferroptosis in cancer. *Nat Rev Clin Oncol*. 2021;18(5):280–296. doi:10.1038/s41571-020-00462-0
27. Tang D, Chen X, Kang R, Kroemer G. Ferroptosis: molecular mechanisms and health implications. *Cell Res*. 2021;31(2):107–125. doi:10.1038/s41422-020-00441-1
28. Yan HF, Zou T, Tuo QZ, et al. Ferroptosis: mechanisms and links with diseases. *Signal Transduction Target Therapy*. 2021;6(1):49. doi:10.1038/s41392-020-00428-9
29. Stockwell BR, Jiang X, Gu W. Emerging mechanisms and disease relevance of ferroptosis. *Trends Cell Biol*. 2020;30(6):478–490. doi:10.1016/j.tcb.2020.02.009
30. Lei G, Zhuang L, Gan B. The roles of ferroptosis in cancer: tumor suppression, tumor microenvironment, and therapeutic interventions. *Cancer Cell*. 2024;42(4):513–534. doi:10.1016/j.ccell.2024.03.011
31. Wang Y, Wu X, Ren Z, et al. Overcoming cancer chemotherapy resistance by the induction of ferroptosis. *Drug Resistance Updates*. 2023;66:100916. doi:10.1016/j.drup.2022.100916
32. Cai J, Xu X, Saw PE. Nanomedicine targeting ferroptosis to overcome anticancer therapeutic resistance. *Science China Life Sciences*. 2024;67(1):19–40. doi:10.1007/s11427-022-2340-4
33. Wu M, Ling W, Wei J, et al. Biomimetic photosensitizer nanocrystals trigger enhanced ferroptosis for improving cancer treatment. *J Control Release*. 2022;352:1116–1133. doi:10.1016/j.jconrel.2022.11.026
34. He Z, Zhou H, Zhang Y, et al. Oxygen-boosted biomimetic nanoplatform for synergetic phototherapy/ferroptosis activation and reversal of immune-suppressed tumor microenvironment. *Biomaterials*. 2022;290:121832.
35. Guo R, Deng M, Li J, et al. Depriving tumor cells of ways to metastasize: ferroptosis nanotherapy blocks both hematogenous metastasis and lymphatic metastasis. *Nano Lett*. 2023;23(8):3401–3411. doi:10.1021/acs.nanolett.3c00365
36. Chen Y, Yao Z, Liu P, et al. A self-assembly nano-prodrug for triple-negative breast cancer combined treatment by ferroptosis therapy and chemotherapy. *Acta Biomater*. 2023;159:275–288. doi:10.1016/j.actbio.2023.01.050
37. Lin Z, Song J, Gao Y, et al. Hypoxia-induced HIF-1 α /lncRNA-PMAN inhibits ferroptosis by promoting the cytoplasmic translocation of ELAVL1 in peritoneal dissemination from gastric cancer. *Redox Biol*. 2022;52:102312. doi:10.1016/j.redox.2022.102312
38. Fuhrmann DC, Mondorf A, Beifuß J, Jung M, Brüne B. Hypoxia inhibits ferritinophagy, increases mitochondrial ferritin, and protects from ferroptosis. *Redox Biol*. 2020;36:101670. doi:10.1016/j.redox.2020.101670
39. Xiong Z, Sun B, Zou H, et al. Amorphous-to-crystalline transformation: general synthesis of hollow structured covalent organic frameworks with high crystallinity. *J Am Chem Soc*. 2022;144(14):6583–6593. doi:10.1021/jacs.2c02089
40. Li M, Li X, Cao Z, et al. Mitochondria-targeting BODIPY-loaded micelles as novel class of photosensitizer for photodynamic therapy. *Eur J Med Chem*. 2018;157:599–609. doi:10.1016/j.ejmech.2018.08.024
41. Zhang Y, Feng S, Hu G, et al. An adenovirus-mimicking photoactive nanomachine preferentially invades and destroys cancer cells through hijacking cellular glucose metabolism. *Adv Funct Mater*. 2021;32(13):2110092.
42. Yu Y, Tang D, Liu C, et al. Biodegradable polymer with effective near-infrared-ii absorption as a photothermal agent for deep tumor therapy. *Adv Mater*. 2021;34(4):2105976.
43. Xiong J, Wu M, Chen J, et al. Cancer-erythrocyte hybrid membrane-camouflaged magnetic nanoparticles with enhanced photothermal-immunotherapy for ovarian cancer. *ACS nano*. 2021;15(12):19756–19770. doi:10.1021/acs.nano.1c07180
44. Cheung EC, Vousden KH. The role of ROS in tumour development and progression. *Nat Rev Cancer*. 2022;22(5):280–297. doi:10.1038/s41568-021-00435-0
45. Chen C, Wang D, Yu Y, et al. Legumain promotes tubular ferroptosis by facilitating chaperone-mediated autophagy of GPX4 in AKI. *Cell Death Dis*. 2021;12(1):65. doi:10.1038/s41419-020-03362-4
46. Kalyane D, Raval N, Maheshwari R, Tambe V, Kalia K, Tekade RK. Employment of enhanced permeability and retention effect (EPR): nanoparticle-based precision tools for targeting of therapeutic and diagnostic agent in cancer. *Mater Sci Eng C Mater Biol Appl*. 2019;98:1252–1276. doi:10.1016/j.msec.2019.01.066
47. Sun N, Wen X, Zhang SA-O. Strategies to improve photodynamic therapy efficacy of metal-free semiconducting conjugated polymers. *Int J Nanomed*. 2022;Volume 17:247–271. doi:10.2147/IJN.S337599
48. Feng L, Zhu C, Yuan H, Liu L, Lv F, Wang S. Conjugated polymer nanoparticles: preparation, properties, functionalization and biological applications. *Chem Soc Rev*. 2013;42(16):6620. doi:10.1039/c3cs60036j
49. Feng G, Zhang Gq Fau - Ding D, Ding D. Design of superior phototheranostic agents guided by Jablonski diagrams. *Chemical Society Reviews*. 2020;49(22):8179–8234. doi:10.1039/D0CS00671H
50. Zhou LL, Guan Q, Li WY, Zhang Z, Li YA, Dong YB. A ferrocene-functionalized covalent organic framework for enhancing chemodynamic therapy via redox dyshomeostasis. *Small*. 2021;17(32). doi:10.1002/sml.202101368
51. Zhang L, Song A, Yang Q-C, et al. Integration of AIEgens into covalent organic frameworks for pyroptosis and ferroptosis primed cancer immunotherapy. *Nat Commun*. 2023;14(1):5355. doi:10.1038/s41467-023-41121-z
52. You J, Yuan F, Cheng S, et al. AIEgen-based sp² carbon-conjugated covalent organic frameworks with high stability and emission for activatable imaging and ferroptosis in target tumor cells. *Chem Mater*. 2022;34(15):7078–7089. doi:10.1021/acs.chemmater.2c01726
53. Zhang S, Xia S, Chen LA-O, Chen YA-O, Zhou J. Covalent organic framework nanobowls as activatable nanosensitizers for tumor-specific and ferroptosis-augmented sonodynamic therapy. *Advanced Science*. 2023;10(6). doi:10.1002/advs.202206009
54. Zhang LF, Yang -L-L, Yang LF, et al. Three-dimensional covalent organic frameworks with cross-linked pores for efficient cancer immunotherapy. *Nano Letters*. 2021;21(19):7979–7988. doi:10.1021/acs.nanolett.1c02050
55. Zhang LA-O, Yang QC, Wang S, et al. Engineering multienzyme-mimicking covalent organic frameworks as pyroptosis inducers for boosting antitumor immunity. *Advanced Materials*. 2022;34(13):2108174.
56. Kalliolias GD, Ivashkiv LB. TNF biology, pathogenic mechanisms and emerging therapeutic strategies. *Nature Reviews Rheumatology*. 2016;12(1):49–62. doi:10.1038/nrrheum.2015.169
57. Blaser H, Dostert C, Mak TW, Brenner D. TNF and ROS Crosstalk in Inflammation. *Trends in Cell Biology*. 2016;26(4):249–261. doi:10.1016/j.tcb.2015.12.002

International Journal of Nanomedicine

Dovepress

Publish your work in this journal

The International Journal of Nanomedicine is an international, peer-reviewed journal focusing on the application of nanotechnology in diagnostics, therapeutics, and drug delivery systems throughout the biomedical field. This journal is indexed on PubMed Central, MedLine, CAS, SciSearch®, Current Contents®/Clinical Medicine, Journal Citation Reports/Science Edition, EMBase, Scopus and the Elsevier Bibliographic databases. The manuscript management system is completely online and includes a very quick and fair peer-review system, which is all easy to use. Visit <http://www.dovepress.com/testimonials.php> to read real quotes from published authors.

Submit your manuscript here: <https://www.dovepress.com/international-journal-of-nanomedicine-journal>